COMPUTER RESEARCH AND MODELING
2026 VOL. 18 NO. 3 P. e715–e735
DOI: 10.20537/2076-7633-2026-18-3-715-735

Ки&М

SPECIAL ISSUE

UDC: 519.6:616.132.2-073.756.5

Method for coronary blood flow velocity estimation based on angiographic images

A. A. Rebrova[1,a], A. A. Danilov[1,2,3,b]

[1]Marchuk Institute of Numerical Mathematics RAS,
8 Gubkina st., Moscow, 119333, Russia
[2]Moscow Institute of Physics and Technology (National Research University),
9 Institutskii per., Dolgoprudny, 141700, Russia
[3]Sechenov First Moscow State Medical University,
8/2 Trubetskaya st., Moscow, 119048, Russia

E-mail: [a] lina.rebrova@yandex.ru, [b] a.danilov@inm.ras.ru

Received 10.04.2026, after completion — 23.04.2026.
Accepted for publication 23.04.2026.

In modern cardiology, accurate assessment of the functional significance of coronary artery stenoses is a critical factor for selecting treatment strategies and making informed clinical decisions. This paper presents an automated algorithm for processing dynamic X-ray angiographic image sequences aimed at estimating blood flow velocity. This parameter serves as the basis for determining the Quantitative Flow Ratio (QFR), which acts as an effective noninvasive alternative to traditional invasive fractional flow reserve (FFR) measurements. The proposed methodology successfully overcomes classic challenges of angiographic analysis, such as vessel motion artifacts during the cardio-respiratory cycle, variable contrast opacification, and the geometric complexity of the vascular tree in two-dimensional projections.

The presented processing workflow includes several key stages. Initially, frame preprocessing is performed to suppress noise and filter out the anatomical background. Subsequently, segmentation is implemented using a Sato filter and Otsu thresholding, followed by skeletonization to extract vessel centerlines. Particular attention is paid to the algorithm for automated identification of bifurcation points and the filtration of artifactual intersections caused by vessel overlapping. To ensure data continuity, a temporal tracking method for the target segment based on template correlation is applied, which is especially important during phases with low contrast agent concentration. The mathematical core of the algorithm is based on solving a 1D inverse problem for the advection-diffusion equation, allowing for the recovery of blood flow velocity from temporal intensity curves.

As part of the study, a detailed validation of the method was conducted by comparing automated calculation results with manual expert measurements across ten clinical datasets. The results confirm the robustness of the computational scheme within physiologically relevant ranges and its ability to significantly reduce inter-observer variability. The developed approach minimizes the need for physician intervention in the data processing stage, opening up prospects for creating real-time clinical decision support systems in the catheterization laboratory setting.

Keywords: medical image segmentation, coronary circulation, fractional flow reserve, coronary flow reserve, quantitative flow ratio, angiography, blood flow velocity, inverse problems, numerical methods

Citation: *Computer Research and Modeling*, 2026, vol. 18, no. 3, pp. e715–e735.

This work was supported by the Moscow Center of Fundamental and Applied Mathematics at INM RAS (Agreement with the Ministry of Science and Higher Education of the Russian Federation No. 075-15-2025-347).

КОМПЬЮТЕРНЫЕ ИССЛЕДОВАНИЯ
И МОДЕЛИРОВАНИЕ 2026 Т. 18 № 3 С. e715–e735
DOI: 10.20537/2076-7633-2026-18-3-715-735

Ки&М

СПЕЦИАЛЬНЫЙ ВЫПУСК

УДК: 519.6:616.132.2-073.756.5

Метод оценки скорости коронарного кровотока по ангиографическим изображениям

А. А. Реброва[1,a], А. А. Данилов[1,2,3,b]

[1]Институт вычислительной математики им. Г. И. Марчука РАН,
Россия, 119333, г. Москва, ул. Губкина, д. 8
[2]Московский физико-технический институт (национальный исследовательский университет),
Россия, 141700, г. Долгопрудный, пер. Институтский, д. 9
[3]Первый МГМУ им. И. М. Сеченова Минздрава России (Сеченовский университет),
Россия, 119048, г. Москва, ул. Трубецкая, д. 8, стр. 2

E-mail: [a] lina.rebrova@yandex.ru, [b] a.danilov@inm.ras.ru

Получено 10.04.2026, после доработки — 23.04.2026.
Принято к публикации 23.04.2026.

В современной кардиологии точная оценка функциональной значимости стенозов коронарных артерий является критическим фактором для выбора тактики лечения и принятия обоснованных клинических решений. В данной работе представлен автоматизированный алгоритм для обработки динамических последовательностей рентгеновских ангиографических изображений, направленный на оценку скорости кровотока. Данный параметр служит основой для определения количественного соотношения кровотока (QFR), выступающего эффективной неинвазивной альтернативой традиционному инвазивному измерению фракционного резерва кровотока. Предложенная методика успешно преодолевает классические трудности ангиографического анализа, такие как артефакты движения сосудов в ходе сердечно-дыхательного цикла, неравномерная контрастная плотность и геометрическая сложность сосудистого дерева в двумерных проекциях.

Представленный алгоритм обработки включает в себя несколько ключевых стадий. Первоначально выполняется предобработка кадров для подавления шумов и фильтрации анатомического фона. Далее проводится сегментация с использованием фильтра Сато и пороговой обработки Оцу, после чего производится скелетонизация для извлечения центральных линий сосудов. Особое внимание уделено алгоритму автоматической идентификации точек бифуркации и фильтрации артефактных пересечений, возникающих при наложении сосудов. Для обеспечения непрерывности данных применяется метод временного отслеживания целевого сегмента на основе корреляции шаблонов, что особенно важно в фазах с низкой концентрацией контрастного вещества. Математическое ядро алгоритма основано на решении обратной одномерной задачи для уравнения адвекции – диффузии, что позволяет восстановить скорость кровотока по временным кривым интенсивности.

В рамках исследования проведена детальная валидация метода путем сопоставления результатов автоматического расчета с ручными экспертными измерениями на десяти наборах клинических данных. Полученные результаты подтверждают устойчивость вычислительной схемы в физиологически значимых диапазонах и ее способность значительно снижать межэкспертную вариабельность. Разработанный подход минимизирует необходимость врачебного вмешательства в процесс обработки данных, открывая перспективы для создания систем поддержки принятия врачебных решений в реальном времени в условиях катетеризационной лаборатории.

Ключевые слова: сегментация медицинских изображений, коронарное кровообращение, фракционный резерв кровотока, резерв коронарного кровотока, количественное соотношение кровотока, ангиография, скорость кровотока, обратные задачи, численные методы

Работа выполнена при поддержке Московского центра фундаментальной и прикладной математики в ИВМ РАН (Соглашение с Министерством науки и высшего образования Российской Федерации № 075-15-2025-347).

Introduction

In modern cardiology, the accurate assessment of the functional significance of coronary artery stenoses is a critical factor for making informed clinical decisions. The gold standard for this assessment has long been the invasive measurement of the Fractional Flow Reserve (FFR), which requires the use of expensive pressure-wire sensors [Conte et al., 2020]. An alternative noninvasive technique derived from computed tomography (CT) data is virtual FFR (vFFR) — a technology based on a 3D model of the coronary arteries, and application of the physical laws of fluid flow [Pantos, Katritsis, 2014; Tu et al., 2014; Haley et al., 2021]. Virtual FFR offers clinical advantages such as lower patient risk, no requirement for catheterization, and the capability for both anatomical and physiological assessment within a single study. This allows for a more effective determination of revascularization strategy and prediction of long-term outcomes better than using CT angiography alone [Ihdayhid et al., 2019; Zhuang et al., 2019; Guan et al., 2023]. Limitations of the method include variability in diagnostic performance depending on stenosis severity, significant data processing time, and the need for high-quality images; some approaches also require high-performance computing resources or machine learning algorithms [Ko et al., 2017; Tesche et al., 2018]. Compared to invasive FFR, non-invasive virtual FFR cannot yet fully replace direct measurements in all cases, however, it serves as a valuable preliminary screening tool, allowing the number of unnecessary invasive procedures to be reduced while maintaining a high level of diagnostic accuracy [Guan et al., 2023; Peters et al., 2024].

Another non-invasive approach is the Quantitative Flow Ratio (QFR) — a non-invasive method based on the analysis of standard X-ray angiographic sequences [Saito et al., 1990; Chu et al., 2022]. Its accuracy and clinical applicability directly depend on the reliability of automated image processing algorithms, which must ensure correct analysis of the temporal dynamics of contrast agent propagation. Angiography-based quantitative flow ratio (QFR) shows high diagnostic accuracy in identifying hemodynamically significant coronary stenosis compared to invasive fractional flow reserve (FFR), with sensitivity and specificity often exceeding 85–90 % in multiple studies [Xu et al., 2017; Westra et al., 2018a; Westra et al., 2018b]. QFR offers a less invasive alternative that can be computed rapidly during coronary angiography, improving procedural feasibility and reducing time compared to FFR [Westra et al., 2018a; O'Brien et al., 2023]. However, in a large randomized trial (FAVOR III Europe), QFR-guided revascularization was inferior to FFR-guided strategy for 12-month outcomes, suggesting that FFR remains the preferred method when available [Andersen et al., 2024]. Diagnostic concordance between QFR and FFR is strong even in complex coronary artery disease, although lesion location may influence agreement [Kawashima et al., 2022]. In calcified lesions, a Murray law-based QFR variant (μQFR) shows moderate diagnostic accuracy but somewhat lower sensitivity and specificity than in noncalcified vessels [Bennar et al., 2025]. Overall, QFR demonstrates good diagnostic performance but is not yet a complete replacement for invasive FFR [Xu et al., 2017; Westra et al., 2018a; Westra et al., 2018b; Andersen et al., 2024].

Recent advances in deep learning have significantly improved automated coronary artery segmentation in X-ray angiography, addressing challenges such as low contrast, motion artifacts, and overlapping structures. Models like the Temporal Vessel Segmentation Network (TVS-Net) leverage temporal information from sequential frames to achieve high accuracy (Dice scores around 83–86 %) and robustness across datasets [He et al., 2025]. Fully convolutional networks trained on large datasets have demonstrated real-time segmentation with high F1 scores (~ 0.92), effectively capturing stenotic regions and vessel connectivity [Yang et al., 2019]. Ensemble methods combining deep learning with filter-based features also show strong performance, achieving F1 scores near 0.87 and high specificity, which aids in accurate stenosis assessment [Gao et al., 2022]. Attention mechanisms, multiscale context fusion, and lightweight architectures further enhance segmentation accuracy while reducing

computational costs, with sensitivity and specificity often exceeding 80–90 % [Algarni et al., 2022; Li, Fan, 2024; Tao et al., 2022; Zhang et al., 2023]. Additionally, some approaches integrate preprocessing techniques like contrast enhancement and post-processing refinement to improve vessel continuity and reduce false positives, supporting more reliable clinical diagnosis and treatment planning [Hassan et al., 2025; Nobre Menezes et al., 2023]. However, automated blood flow velocity estimation using deep learning in X-ray angiography remains less explored in these studies.

The computation of QFR necessitates personalized data, including vascular geometry, as well as pressure and velocity profiles. While the geometry is typically reconstructed from biplane angiographic projections and pressure can be obtained via direct or indirect measurements, velocity estimation remains a more complex task. Conventional approaches to velocity assessment include frame counting, bolus tracking [Zhang et al., 2018; Sokolov et al., 2019], and transit time analysis [Wu et al., 2022]. In our study, we propose an alternative velocity estimation technique based on the formulation and solution of an inverse one-dimensional transport problem. The technique for inverse problem solution was proposed by V. I. Vasilev et al. [Васильев и др., 2026].

The key technological challenge in implementing QFR is the processing of angiographic data, which includes vessel segmentation, reconstruction of their centerlines, identification of characteristic points (such as bifurcations), and, most importantly, temporal analysis to determine blood flow velocity. This process is complicated by several factors: vessel motion due to cardiac and respiratory artifacts, low structural visibility in noncontrast phases, and complex cases of vessel geometry involving self-intersections on projection planes. Traditional processing methods often require manual correction.

This article describes a comprehensive algorithmic approach to the automated processing of angiographic images for QFR calculation. The presented methodology covers the full pipeline: from the data preprocessing and vessel segmentation stage to the extraction of centerlines, temporal analysis of contrast propagation, and direct calculation of blood flow velocity. The goal of this work is to create a robust tool capable of minimizing the need for physician intervention during the analysis stage and improving the accuracy of non-invasive assessment of hemodynamic impairments, which holds significant potential for widespread adoption in clinical practice.

Velocity identification in 1D transport model

The evolution of the contrast agent concentration $C(x, t)$ in a one-dimensional vessel segment $x \in [0, L]$ is governed by the advection-diffusion equation:

$$\frac{\partial C}{\partial t} + V\frac{\partial C}{\partial x} - D\frac{\partial^2 C}{\partial x^2} = 0, \quad x \in (0, L),\ t \in (0, T], \tag{1}$$

where $V(t)$ represents the flow velocity to be identified, and D is the effective longitudinal diffusion coefficient. In our work we assume that the diffusion coefficient D is constant, and the velocity $V(t)$ is the same along the entire segment and depends only on time. The system is supplemented with the initial condition $C(x, 0) = C_0(x)$, representing an initial concentration in the vessel prior to injection, and the observed inflow and outflow boundary conditions $C(0, t) = g_0(t)$, $C(L, t) = g_1(t)$, which describe the contrast agent profile.

The forward problem consists of finding $C(x, t)$ given a known velocity $V(t)$. In this study, we consider the inverse coefficient problem where the velocity is unknown and must be recovered from experimental observations. We assume that the concentration is known at the initial time, and is also monitored at the inlet and outlet of the vessel, providing the measured data $C_0(x)$, $g_0(t)$, and $g_1(t)$. We

also assume that an additional integral overdetermination condition is used:

$$\int_0^L C(x,\, t)\, dx = \Phi(t). \tag{2}$$

The inverse problem is thus defined as finding a parameter $V(t)$ such that the solution to the transport equation (1) matches the observed integral overdetermination condition (2).

In our work we use the computational technique for the inverse problem solution proposed by V. I. Vasilev et al. from Ammosov North-Eastern Federal University and presented at the Sixth International Conference "Supercomputer Technologies of Mathematical Modelling" in July, 2025 [Васильев и др., 2026]. The technique is based on the decomposition of the solution similar to that proposed in the previous work [Вабищевич, Васильев, 2014]. We briefly outline this computational technique below with minor changes in the notation used and accounting for the diffusion coefficient D. For simplicity, we assume that the effective longitudinal diffusion coefficient D is constant.

Consider the finite difference approximation $y_i^j = C(x_i,\, t_j)$ on the uniform grid $x_i = ih$, where $h = \frac{L}{N}$, and $t_j = j\tau$, where $\tau = \frac{T}{M}$. The semi-implicit scheme for the transport problem (1) gives:

$$\frac{y_i^j - y_i^{j-1}}{\tau} + V^j \frac{y_i^{j-1} - y_{i-1}^{j-1}}{h} - D\frac{y_{i+1}^j - 2y_i^j + y_{i-1}^j}{h^2} = 0, \quad i = 1,\, 2,\, \ldots,\, N-1,\ j = 1,\, 2,\, \ldots,\, M, \tag{3}$$

$$y_0^j = g_0(t_j), \quad y_N^j = g_1(t_j), \quad j = 1,\, 2,\, \ldots,\, M, \tag{4}$$

$$y_i^0 = C_0(x_i), \quad i = 0,\, 1,\, \ldots,\, N. \tag{5}$$

The integral overdetermination condition gives:

$$\sum_{i=0}^{N} y_i^j \hbar_i = \Phi(t_j), \quad j = 0,\, 1,\, \ldots,\, M, \tag{6}$$

where

$$\hbar_i = \begin{cases} h, & i = 1,\, 2,\, \ldots,\, N-1, \\ \dfrac{h}{2} & \text{otherwise.} \end{cases}$$

Introducing constants $r = \frac{h^2}{D\tau}$, $c = r + 2$ and $g = \frac{h}{D}$, one can rewrite (3) at time step τ_j in the following form (with the signs of the expressions reversed):

$$y_{i-1}^j - cy_i^j + y_{i+1}^j + ry_i^{j-1} - V^j g\left(y_i^{j-1} - y_{i-1}^{j-1}\right) = 0, \quad i = 1,\, 2,\, \ldots,\, N-1, \tag{7}$$

$$y_0^j = g_0(\tau_j), \quad y_N^j = g_1(\tau_j).$$

Next, one can decompose the solution in the following form:

$$y_i^j = V^j w_i^j + z_i^j, \quad i = 0,\, 1,\, \ldots,\, N. \tag{8}$$

Using this decomposition, equation (7) gives

$$V^j\left\{w_{i-1}^j - cw_i^j + w_{i+1}^j - g\left(y_i^{j-1} - y_{i-1}^{j-1}\right)\right\} + \left\{z_{i-1}^j - cz_i^j + z_{i+1}^j + ry_i^{j-1}\right\} = 0, \quad i = 1,\, 2,\, \ldots,\, N-1. \tag{9}$$

If both expressions in braces are zero, then the whole expression will be zero as well. So, a sufficient condition for the solution of (9) is a pair of two linear systems with the same tridiagonal matrix:

$$\begin{cases} w_{i-1}^j - cw_i^j + w_{i+1}^j = g\left(y_i^{j-1} - y_{i-1}^{j-1}\right), & i = 1, 2, \ldots, N-1,\ w_0 = w_N = 0, \\ z_{i-1}^j - cz_i^j + z_{i+1}^j = -ry_i^{j-1}, & i = 1, 2, \ldots, N-1,\ z_0 = g_0(\tau_j),\ z_N = g_1(\tau_j). \end{cases} \tag{10}$$

The velocity V^j is computed from the integral overdetermination condition (6) as follows:

$$V^j = \frac{\Phi^j - \sum\limits_{i=0}^{N} z_i \hbar_i}{\sum\limits_{i=0}^{N} w_i \hbar_i}. \tag{11}$$

In summary, the general procedure proposed by V. I. Vasilev et al. for solving the inverse problem to identify the velocity satisfying equations (1) and (2) can be outlined as follows: at each time step solve linear systems with tridiagonal matrix (10) using the boundary conditions (4) for right-hand sides and the initial condition (5) for the first time step, then compute velocity using (11), and update the solution using (8).

In order to utilize the described algorithm, we need to extract the following data from the medical images:

1) The length L of the vessel segment.
2) The initial concentration $C_0(x)$ along the vessel segment on the uniform grid, see (5).
3) The concentration profiles $g_0(t)$ and $g_1(t)$ for inlet and outlet boundary conditions, see (4).
4) The integral concentration profile $\Phi(t)$ over the whole vessel segment as the integral overdetermination condition, see (2).

In this paper we also compare our results with a more classical approach using the center of gravity method [Wu et al., 2022]. The latter approach does not require the integral concentration profile $\Phi(t)$, and the velocity is simply estimated as $V_{\text{TCG}} = \frac{L}{t_{\text{CG1}} - t_{\text{CG0}}}$, where the contrast agent arrival times $t_{\text{CG}*}$ are computed as the center of gravity of the concentration profiles $g_*(t)$ for the inlet and outlet of the vessel segment, i. e.,

$$t_{\text{CG}*} = \frac{\int\limits_0^T g_*(t) t\, dt}{\int\limits_0^T g_*(t)\, dt}. \tag{12}$$

Angiographic image segmentation

The implementation of the proposed numerical method for blood flow velocity identification requires the extraction of input parameters from sequences of angiographic frames. The mathematical formulation of the inverse problem (1)–(2) relies on the values of the length of the considered segment L, the boundary conditions $g_0(t)$ and $g_1(t)$, as well as the integral overdetermination condition $\Phi(t)$ and the initial concentration distribution $C_0(x)$. In this section, we describe automatic algorithms for vessel segmentation and tracking on angiographic images. The automation of obtaining

these characteristics will allow minimizing the influence of noise and motion artifacts on the formation of the computational domain. To this end, the proposed approach combines the stages of image intensity calibration, morphological processing, and tracking of the vascular tree by characteristic points.

The complete algorithm for automated blood flow velocity determination can be represented as the following sequence of steps:

1) Image preprocessing.

2) Vessel segmentation.

3) Vascular branching points detection.

4) Vessel detection on all time frames.

5) Calculation of contrast agent concentration in vessels.

6) Calculation of blood flow velocity.

The input data is a sequence of X-ray angiographic frames capturing the passage of contrast agent through the coronary arteries.

During the preprocessing step (Step 1), a time-averaged image is computed for each set of angiographic frames (Fig. 1). This average image represents the stationary anatomical background (such as bones and other tissues) and the baseline vessel appearance without contrast. By subtracting this average image from each frame, we significantly reduce noise and artifacts unrelated to contrast dynamics, thereby enhancing the reliability of the subsequent analysis.

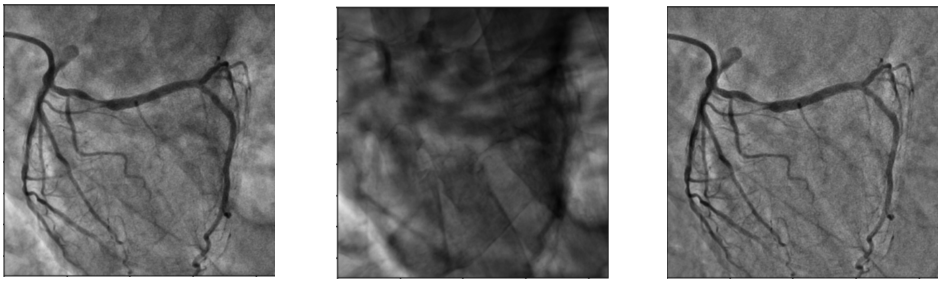

(a) (b) (c)

Figure 1. Preprocessing steps: (a) initial data, frame No. 72, (b) time-averaged angiographic image (156 frames total), (c) data after processing, frame No. 72

At Step 2 the vessels are segmented. For each frame of the normalized image a multiscale vessel enhancement filter (Sato filter [Sato et al., 1998]) is applied, which highlights tubular structures of a given radius r. This filter computes a response for a given range of radii r, corresponding to the expected range of vessel diameters in the image. The r values were selected discretely in the range from $r_{\min}$ to $r_{\max}$, expressed in pixels. The lower bound $r_{\min}$ = 0.8 mm corresponds to the finest visible vessels, while the upper bound $r_{\max}$ = 2.5 mm corresponds to the widest ones. The final filter response for each pixel is defined as the maximum response across all scales r.

The resulting vesselness response $W(x, y, t)$ is then binarized using the Otsu thresholding [Otsu, 1979] method. To eliminate small gaps and noise inclusions, a morphological closure operation is applied to the binary mask using a disk-shaped structural element with a radius of 0.5 mm. This radius was chosen empirically as a compromise between the efficiency of connecting closely spaced vessel segments and minimizing distortion of their geometry to obtain the final binary vessel mask M_t

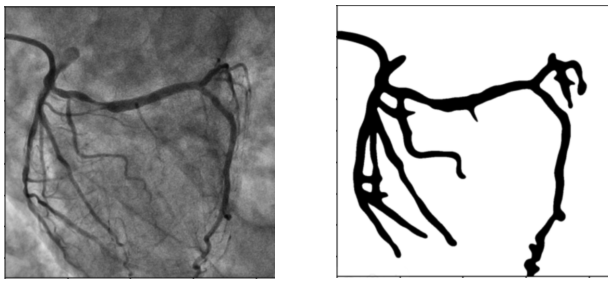

(a) (b)

Figure 2. Vessel segmentation: (a) initial data, (b) binary segmentation

(Fig. 2). Even after preprocessing, the resulting composite mask may still contain multiple disconnected components. This occurs due to inherent image noise, nonuniform contrast distribution within the vessel lumen, and temporal variations in contrast visibility where certain segments may appear discontinuous between frames.

The extracted binary masks are used to automatically reconstruct vessel centerlines and identify vascular bifurcation points.

From each binary vessel mask M_t, we compute the vessel centerlines using a skeletonization algorithm [Lü, Wang, 1986]. Skeletonization reduces the binary vessel regions to one-pixel-wide centerlines S_t, effectively capturing the median paths of the vessels. These centerlines form a graph of connected segments, where end points correspond to vessel terminals and junctions in the skeleton correspond to branch points in the vessel network. We detect all branch points on the skeleton S_t by finding pixels that have more than two neighbors on the centerline (i. e., where a vessel splits into two or more branches) (Fig. 3).

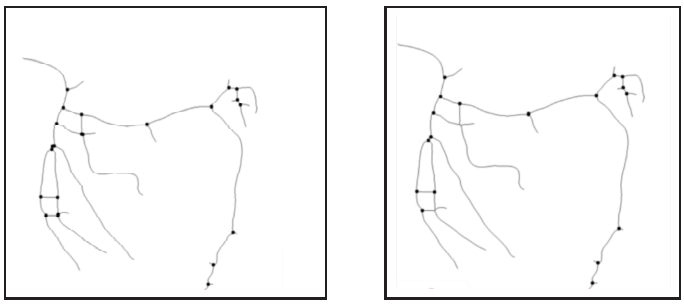

(a) (b)

Figure 3. Extraction of the vessel centerline and branch points: (a) all bifurcation points, (b) points that appear to have multiple crossing segments are excluded from the branch point set

Typically, a bifurcation in a tree structure will appear as a skeleton junction with 3 connected segments (a single parent vessel splitting into two children). However, in a 2D projection, different vessels can overlap, producing a crossing that might also appear as a connected junction in the skeleton.

To distinguish true branch points of the vessel from artifactual crossings, for each candidate point p on the vessel centerline, a square neighborhood $N(p)$ of fixed size (e. g., 9×9 pixels) is defined. The binary vessel mask within $N(p)$ is analyzed to determine how it partitions the entire neighborhood area into distinct background regions.

A point p is classified as a self-intersection point if the vessel structure divides $N(p)$ into four or more such background regions. If a skeleton junction has four or more connected segments, it is

likely a projection of two vessels crossing each other rather than a single anatomical bifurcation. Our algorithm identifies such junctions and removes them or marks them as nonbranch intersections. By filtering out these high-degree nodes, we obtain a set of genuine branch points B_t for each frame t, which represent actual bifurcations in the coronary tree (Fig. 3).

In order to focus on the specific vessel segment that contains the stenosis of interest, we isolate that vessel from the full vascular network. We assume that the proximal (upstream) and distal (downstream) endpoints of the target vessel segment are known or can be selected (for example, by user input or by using clinical knowledge of the lesion location).

In order to transition from a dynamic image sequence to a one-dimensional computational model, it is necessary to define a reference state of the vessel segment in which the geometric characteristics are most clearly defined. Using an arbitrary frame for the centerline reconstruction is associated with risks caused by the nonuniform filling of the artery lumen with contrast agent and the presence of noise that distorts the visible boundaries and length of the vessel. Thus, the algorithm includes an automatic search step, which selects the frame with the maximum contrast filling $f_{\max}$. This frame is identified by analyzing the binary vessel masks obtained from the preliminary segmentation of all frames in the sequence. The frame for which the total area of the segmented vessel mask within the region of interest reaches its global maximum is selected. This criterion directly corresponds to the phase of maximum luminal filling by the contrast agent.

We utilize the frame with the maximum contrast fill as a reference, since in that frame the vessel is most clearly visible and easiest to segment. In that frame ($f_{\max}$), we examine the skeleton and branch points to identify the path between the given endpoints. This frame is used to form the reference vessel mask, which is subsequently used both to determine the physical length L and as a basis for the spatio-temporal tracking of the vessel geometry on frames with low or absent contrast visibility.

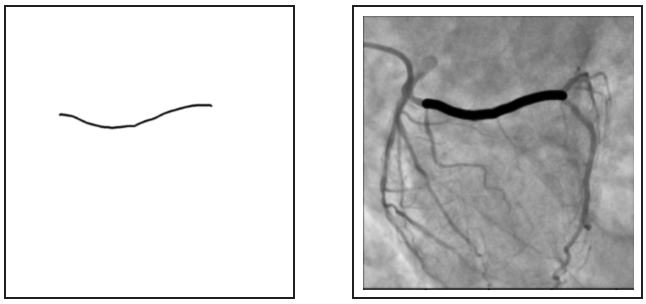

(a) (b)

Figure 4. Identification of the target vessel segment with a stenosis: (a) centerline of target vessel, (b) resulting mask applied to the image

Effectively, we carve out the single vessel of interest from the complex network. Along this path, there may be one or more branch points where side branches diverge. We identify the branch points at or near the endpoints of the chosen segment. In particular, we look for the branch point closest to the proximal endpoint (where the target vessel joins a larger artery) and the branch point closest to the distal endpoint (where the target vessel either ends or gives off a final branch). These two branch points are designated as the *extreme bifurcation points* of the vessel segment. They will serve as key landmarks (characteristic points) for tracking the vessel's motion (Fig. 4). A fixed-width mask is generated by dilating the vessel centerline. The width is selected to slightly exceed the maximum apparent vessel diameter, ensuring complete lumen coverage. This mask is then served as a reference template. During phases of absent contrast, the vessel's trajectory is tracked via motion extrapolation,

and this predefined mask is applied at the predicted locations to maintain a consistent region for signal analysis throughout the temporal sequence.

With the target vessel segment defined on the reference frame $f_{\max}$, the next step is to track this segment through the time sequence. The primary challenge is that the vessel moves over time due to cardiac motion, and in some frames the vessel may be poorly opacified or invisible if contrast has not yet arrived or has cleared. We address this by tracking the positions of the characteristic branch points (such as the two extreme bifurcation points identified above, and possibly additional branch points along the segment) from frame to frame.

Our tracking algorithm works in both directions: starting from the reference frame $f_{\max}$, we track each branch point backward in time (to earlier frames) and forward in time (to later frames). For each branch point in frame t, we search in frame $t - 1$ for the nearest branch point in B_{t-1} that lies within a small neighborhood of the previous location. If a matching point is found (based on minimum distance or a threshold), it is considered to be the same physical point at time $t - 1$. By repeating this for $t - 1$, $t - 2$, and so on, the branch point is followed back to the frame where it either disappears (no match found, perhaps because the vessel is no longer visible) or the beginning of the sequence. A similar procedure is applied forward in time for frames $t + 1$, $t + 2$, etc. This yields a trajectory of each branch point through the sequence.

To ensure continuous vessel tracking in image frames where characteristic bifurcation points were not visible or poorly defined (e. g., due to low contrast or overlapping structures), a template-based tracking approach was employed.

A square region of interest (ROI) containing distinctive local texture was selected from a reference frame where the vessel was clearly visible. In subsequent frames, the position of this ROI was determined by maximizing the normalized cross-correlation coefficient between the reference template and the search area. This method relies on the consistency of local image patterns caused by the vessel wall and surrounding tissues, which remain relatively stable even in the absence of contrast agent [Zaffino et al., 2022]. The calculated displacement vector of the ROI center was used to extrapolate the position of the vessel segment, thereby maintaining tracking continuity throughout the entire angiographic sequence.

This approach effectively “fills in” the vessel segmentation for frames without contrast by leveraging the motion information gleaned from frames with contrast. The result is a complete segmentation of the target vessel across all time frames of the sequence.

After obtaining the spatio-temporal segmentation of the vessel, we analyze the intensity of the contrast agent within the vessel over time to estimate flow characteristics (Step 5). For each frame t, we compute the mean intensity of the pixels inside the segmented vessel region (using the original angiographic frames, not the subtracted ones, so that initial grayscale values are measured). We assume a roughly linear relationship between image intensity and contrast agent concentration for the range of interest.

Next, we convert the measured intensities into quantitative contrast agent concentration values (Fig. 5). A linear mapping is constructed such that the maximum intensity value within the vessel corresponds to zero contrast agent concentration, while the minimum intensity corresponds to a contrast agent concentration of one. This yields an inverse linear relationship between intensity and contrast agent concentration. The mapping is designed in this manner because, as contrast agent flows through the vessel, the corresponding intensity value in the image decreases.

Finally (Step 6), we estimate the blood flow velocity from the temporal contrast curve (Fig. 6). We use the algorithm proposed in the previous section for identification of velocity $V(t)$ from concentration curves $g_0(t)$ and $g_1(t)$ at proximal and distal ends, as well as integral concentration

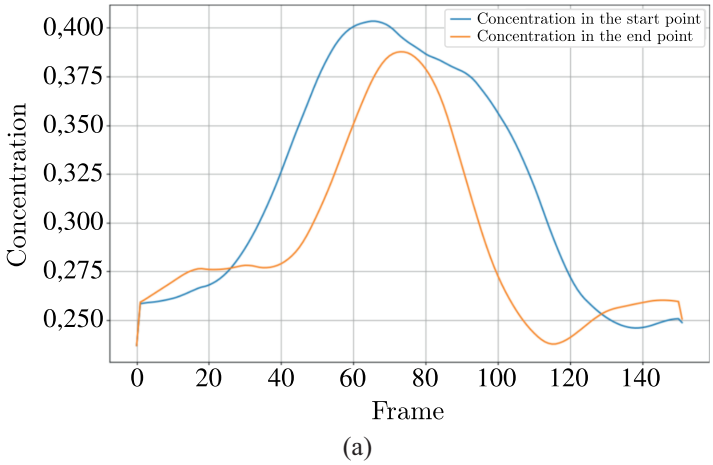

(a)

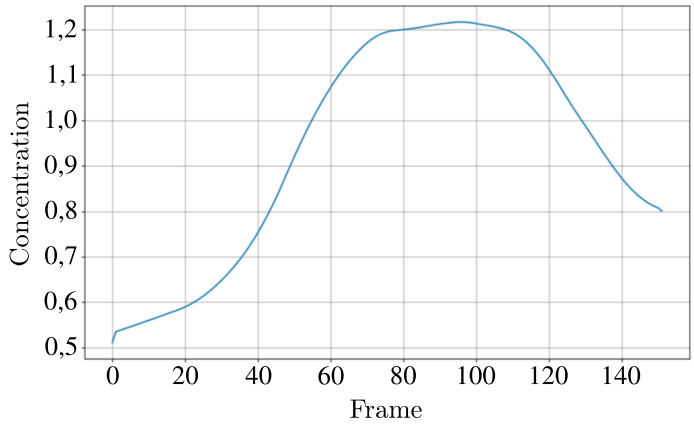

(b)

Figure 5. Measured contrast agent concentrations: (a) contrast agent concentrations at the start point and end point of the vessel over time, (b) integrated contrast agent concentrations in the vessel over time

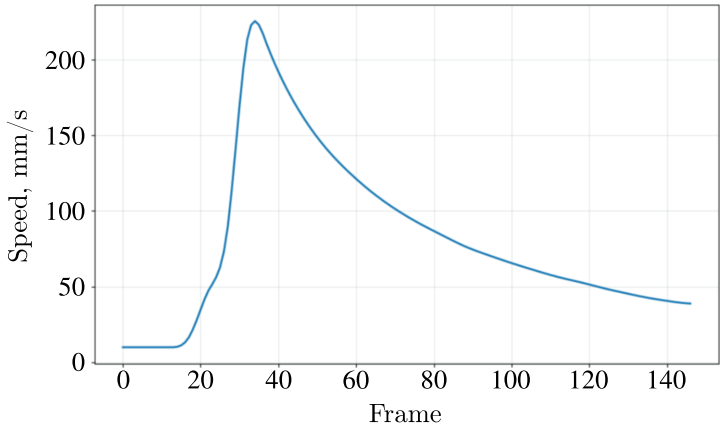

Figure 6. Blood flow velocity

profile $\Phi(t)$ and initial condition $C_0(x)$. Before applying the algorithm, the obtained concentration curves are smoothed by a moving average method with a window width approximately equal to 2–5 % of the total number of frames.

The final blood flow velocity is determined as the time average from the moment of contrast arrival until the moment of complete filling of the target vessel with contrast. Both moments were automatically identified by the algorithm based on the change in mean intensity in the vessel mask: t_{start} is the start of the monotonic increase of intensity (contrast arrival) and t_{max} is the moment when the concentration profile reaches its maximum.

The result of these computations is an estimate of the flow velocity through the stenosed vessel.

Results

This section presents the results of testing the developed automated blood flow velocity estimation algorithm. The primary task of the study is to analyze the sensitivity of the computational scheme to variations in key parameters, such as the segmentation mask width, the diffusion coefficient, as well as the spatio-temporal resolution of the computational grid and the methods of preliminary data smoothing. To minimize the influence of external factors and ensure the reliability of numerical estimates, at the calibration stage the first cycle of computational experiments is conducted on a reference set of angiographic data, characterized by the smallest number of motion artifacts and high quality of contrast bolus visualization. This makes it possible to determine the optimal values of the model parameters that ensure the stability of the solution and the physical plausibility of the results. Subsequently, to confirm the reliability and universality of the proposed approach, an extended study is conducted on a group of patients with various pathologies of the coronary bed, whose data reflect typical clinical variability and the presence of artifacts encountered in everyday clinical practice.

When using various variations of linear mapping between the intensities of the original image and the contrast agent concentration in the one-dimensional problem, the calculated blood flow velocity does not change, due to the linearity of the one-dimensional problem (1)–(2). However, if the original data are used without mapping, that is, the intensity values of the original image are substituted as the concentration in the one-dimensional problem, the resulting velocity becomes negative because the image intensities decrease as the contrast agent accumulates. This suggests that without proper intensity-to-concentration calibration, the velocity computation will yield spurious negative values due to the inverse relationship between intensity and contrast agent concentration.

Let us evaluate the influence of the mask width at the segmentation stage on the calculated blood flow velocity. The mean vessel diameter does not exceed 6–8 mm. If a mask is constructed with a width close to that of the vessel, the velocity does not change significantly. If the mask width is larger, it results in greater smoothing of the initial data, but the outcome remains the same. If the mask is too narrow, it is susceptible to noise and the numerical scheme diverges.

For mask widths of about 8–16 mm (45–100 pixels), the resulting velocity remains approximately 285–289 mm/s. Using a mask larger than the vessel only smooths the data more without changing the outcome. However, a very narrow mask leads to instability: at 35 pixels (5 mm) and at 1 pixel (0.15 mm) the numerical scheme diverges, while intermediate small widths 25 pixels (3.8 mm) or 10 pixels (1.5 mm) produce nonphysical velocities (negative or extremely high) (Table 1).

Let us evaluate the dependence of the calculated blood flow velocity on the diffusion coefficient.

From the presented data, we can see that the calculated blood flow velocity V strongly depends on the diffusion coefficient D. At $D = 14$ mm^2/s the velocity is only 70 mm/s, whereas at $D = 142$ mm^2/s it reaches 1170 mm/s, which is beyond physiological values. According to the literature data [Svitenkov et al., 2018], for coronary arteries a diffusion coefficient in the range 50–100 mm^2/s is typical. This range corresponds to velocities of 285–350 mm/s, which agree well with known physiological norms. Further increase in D leads to a nonphysiological growth of the velocity, indicating a violation of the stability of the numerical scheme or that the model exceeds its applicability limits.

Table 1. Dependence of blood flow velocity on mask width

Mask width (pixels)	Velocity at $D = 50$ mm^2/s (mm/s)
45	285
55	285
65	286
100	289
35	*Scheme diverges*
25	–91
10	330
1	*Scheme diverges*

Table 2. Dependence of blood flow velocity on the diffusion coefficient

D (mm^2/s)	V (mm/s)
14	70
28	130
42	216
50	285
54	293
56	313
71	329
85	347
99	348
113	485
128	529
142	1170

Table 3. The effect of different temporal and spatial resolution settings on the velocity

Simulation setting	Velocity (mm/s)
Without interpolation	285
Time grid 2× finer	282
Spatial grid 2× coarser	321

The table above (Table 3) shows the effect of different temporal and spatial resolution settings on the velocity. The reference case (no interpolation) yields $V \approx 285$ mm/s. A time step twice as fine (half the original step) results in essentially the same velocity 282, indicating the temporal resolution is already sufficient. Using a spatial grid that is twice as coarse (half the spatial resolution) significantly increases the computed velocity (to 321 mm/s). This shows that insufficient spatial resolution can severely distort the results.

Let us evaluate the effect of different methods of smoothing the boundary and initial conditions on the calculated blood flow velocity.

Table 4. Impact of smoothing techniques on calculated blood flow velocity

Smoothing method	Velocity (mm/s)
Without smoothing	323
Moving average (window = 10)	285
Gaussian filter	292
Savitzky – Golay filter (window = 10, order = 3)	287

Applying different smoothing techniques to the data affects the resulting velocity (Table 4). A simple moving average (window length 10, which corresponds to approximately 1 %), which was selected as the default in the processing pipeline, yields a velocity of about 285 mm/s, whereas a Gaussian filter produces a slightly higher velocity (292 mm/s). In contrast, using the Savitzky–Golay filter (window = 10, polynomial order 1) gives a velocity of 287 mm/s. This indicates that the choice of a smoothing method can influence the velocity calculation, probably because each filter handles noise and data trends differently.

When applying smoothing based on a moving average, different window widths also have an influence on the velocity value. In the absence of smoothing, the solution is unstable due to the noise component. With a window width of 10 frames, the solution is smoothed and an initial growth of velocity with subsequent decay is observed. With a window width of 30 frames, the velocity decreases monotonically starting from frame 35. In the case of truncating the sequence to frames with visible contrast, the velocity value turns out to be somewhat underestimated due to the absence of smoothing over the initial frames (Fig. 7).

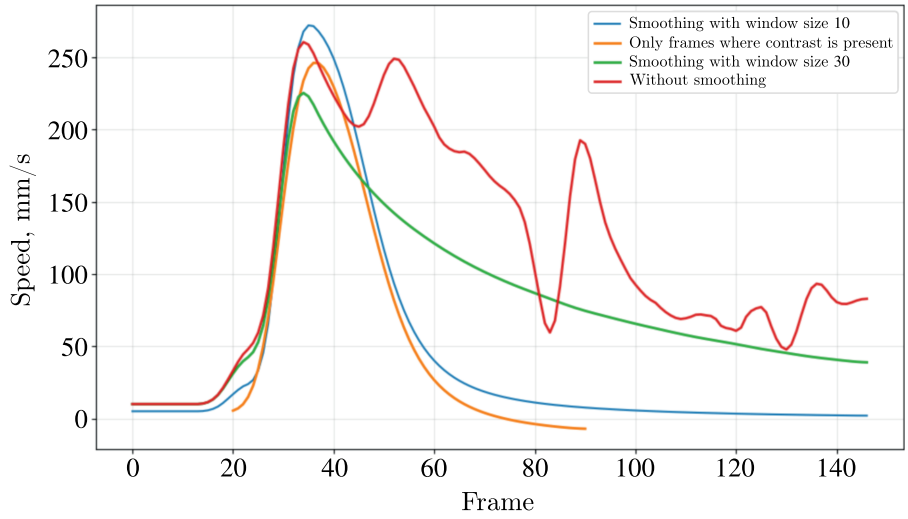

Figure 7. Blood flow velocity calculated with different smoothing parameters: without smoothing, with moving average window sizes of 10 and 30 frames, and using only frames in which contrast propagation occurs

To validate the accuracy of the automated velocity calculation, the results were compared against the manually estimated ones. The manual reference velocity was calculated as the vessel centerline length divided by the contrast transit time, where the transit time was defined as the interval between the arrival of the contrast bolus at the proximal and distal endpoints, determined by visual inspection of the angiographic sequence.

Our automated method yielded a velocity of v = 285 mm/s. The manual measurement for the same dataset yielded $v = 299 \pm 27$ mm/s. The close agreement demonstrates the clinical validity and accuracy of the proposed automated algorithm.

Literature data [Svitenkov et al., 2018] indicate a physiological diffusion coefficient for the left anterior descending (LAD) artery with a mean of 50 mm^2/s and a maximum of 110 mm^2/s. Our simulation parameter D, set to 50 mm^2/s, agrees with the mean value of the clinically observed range, thereby ensuring the physical plausibility of the computed hemodynamic results.

Validation of the developed algorithm was carried out by comparing the calculated blood flow velocity (V_{calc}) with the reference velocity measured manually (V_{man}) for ten anonymized patient datasets. The manually measured velocity was obtained by an expert through frame-by-frame analysis

of contrast agent propagation. The velocity calculated manually by visual estimation (V_{man}) was determined from the same angiographic sequence using the following procedure:

The frame corresponding to the initial arrival of the contrast bolus at the proximal point of the vessel (t_{start}) was identified as the time point where the average intensity profile within the vessel mask began its monotonic increase. The frame of maximum opacification (t_{max}) was identified as the point where this intensity profile reached its global maximum.

The propagation time (Δt) was calculated as the difference in frame indices between t_{start} and t_{max}, multiplied by the known time interval between consecutive frames. The physical length of the vessel segment (L) was measured in millimeters along its centerline.

To account for the inherent uncertainty in precisely identifying the exact start and end frames, a sensitivity analysis was performed. The velocity calculation was repeated with the start frame shifted by ±1 frame. The variation in the resulting velocities provided an estimate of the manual measurement uncertainty. This manually derived V_{man} served as the ground truth for evaluating the accuracy of the fully automated velocity estimation algorithm.

Additionally, two alternative methods were implemented for comparison: the center of the gravity method (V_{TCG}) based on concentration-time curve analysis [Wu et al., 2022], and the visual estimation method $\left(V_{calc_2}\right)$ where the transit time was determined by algorithmic analysis of contrast propagation across frames. For velocity calculation, we recorded the time points at which contrast disappeared at the proximal and distal ends of the vessel segment; the difference between these moments, multiplied by the frame interval, yielded the transit time, and velocity V_{calc_2} was then obtained as vessel length divided by this time.

The results are summarized in Table 5.

Table 5. Comparison of manually measured and algorithm-calculated blood flow velocities (in mm/s) for two projection angles. The diffusion coefficient D = 50 mm^2/s

Patient	Branch	Projection 1				Projection 2			
		V_{calc}	V_{man}	V_{TCG}	V_{calc_2}	V_{calc}	V_{man}	V_{TCG}	V_{calc_2}
1	Left	142	155 ± 15	249	226	285	299 ± 27	350	226
2	Left	332	312 ± 39	110	266	301	298 ± 42	181	259
3	Left	272	305 ± 43	136	192	201	237 ± 23	282	263
4	Right	345	319 ± 45	252	309	321	304 ± 32	332	359
5	Right	115	114 ± 24	270	305	182	215 ± 23	369	257
6	Right	176	210 ± 52	303	432	152	196 ± 65	130	225
7	Left	80	100 ± 30	207	461	83	88 ± 8	146	122
8	Right	303	284 ± 17	351	327	198	245 ± 35	298	287
9	Right	265	294 ± 29	182	218	257	95 ± 6	196	204
10	Left	207	125 ± 5	148	169	168	126 ± 5	192	141

As shown in Table 5, the algorithm demonstrates good agreement with manual measurements.

Discussion and conclusions

This study presents a fully automated algorithm for segmenting coronary vessels in angiographic sequences and deriving hemodynamic parameters critical for calculating the Quantitative Flow Ratio (QFR). The proposed methodology addresses key challenges in angiographic analysis — namely, vessel motion, variable contrast opacification, and complex 2D projections — by integrating temporal tracking, motion extrapolation, and physiologically calibrated intensity analysis.

It is important to note that the blood flow velocity is calculated from individual 2D projections. The projection of the vessel length is usually smaller than the length of the real vessel, which leads to a systematic underestimation of the velocity. When two orthogonal projections are available, the projection lengths may differ significantly. If in one of the projections the vessel turns out to be strongly foreshortened (for example, when imaging along the vessel axis), the calculated velocity will be significantly lower than the true one.

If the velocities calculated from two projections differ significantly, preference should be given to the projection where the velocity is higher. The higher velocity is most likely obtained from the projection with less projection foreshortening, that is, with a more accurate estimation of the vessel length. The underestimated velocity, on the contrary, indicates that the projection turned out to be "short" and does not reflect the real geometry.

In zones with a branched network of vessels and overlapping branches, the accuracy of velocity calculation decreases: the vessel mask captures neighboring structures, which leads to distortion of the concentration curves and incorrect velocity estimation, since pixels not belonging to the target vessel enter the computational region, which is especially critical in the contrast washout phases.

In addition, bifurcation points in the case of self-intersections of vessel projections can be detected with errors, due to which the trajectory of vessel tracking from frame to frame is disrupted.

The velocity analysis in Table 5 shows that the largest discrepancies between V_{calc} and V_{man} are observed in those cases where the projection is characterized by strong vessel foreshortening or a large number of self-intersections. The most illustrative example is patient 9 in the second projection: here the manual estimate (95 mm/s) is more than twice lower than the automated one (257 mm/s). Visual control revealed that the target vessel in this projection practically merges with the background, has many self-intersections, and is overlapped by lateral branches. The algorithm, having no prior information about the anatomy, attempts to extract a connected structure but mistakenly includes neighboring vessels in the mask, which distorts both the segment length and the concentration profile.

It is also worth noting that our one-dimensional problem uses the assumption of a constant velocity $V(t)$ along the vessel. In reality, due to vessel narrowing, the blood flow velocity may vary along the vessel. Similarly, the observed blood flow velocity in a two-dimensional projection will vary as the angle of vessel inclination to the plane changes. Therefore, the velocity values obtained by solving the inverse one-dimensional problem should be interpreted as average values of blood flow velocity along the entire investigated vessel section.

Accurate determination of contrast agent diffusion values, and in particular longitudinal diffusion coefficients in one-dimensional models of blood flow in human coronary arteries, remains a challenging task due to the complex interaction of flow dynamics, vessel geometry, and physiological conditions. Computational fluid dynamics studies show that contrast agent diffusion increases with traveled distance and vessel diameter but decreases with higher flow velocities, causing systematic underestimation errors in myocardial blood flow quantification ranging from about −28 % at rest to −8.5 % under stress [Martens et al., 2019; Martens et al., 2017]. The effective longitudinal diffusion coefficient relevant for coronary arterial blood flow is on the order of 10–100 mm^2/s, as suggested by 1D models accounting for uneven concentration distributions across vessel cross-sections [Svitenkov et al., 2018]. These models incorporate two coupled equations for average concentration and its cross-sectional distribution parameter, capturing realistic propagation dynamics consistent with X-ray angiography patterns [Svitenkov et al., 2018]. Additionally, stenosis severity influences contrast agent transport by altering diffusion and advection coefficients [Alves et al., 2023; Graafen et al., 2011]. Overall, while exact validated numerical values vary depending on modeling assumptions and vessel-specific factors, typical diffusion coefficients around 50 mm^2/s and diffusion effects increasing with

vessel length are supported by current computational studies in coronary arteries [Svitenkov et al., 2018; Martens et al., 2019; Martens et al., 2017].

The strong influence of spatial grid resolution on the results highlights the computational constraints of the method. While temporal refinement had a more subtle effect, significant coarsening of the spatial grid produced nonphysical velocity estimates, emphasizing that the geometric fidelity of the vessel reconstruction is paramount. The moderate variability introduced by different smoothing filters further illustrates that preprocessing choices, while necessary for noise reduction, directly influence the final quantitative output and must be standardized for clinical reproducibility.

A key validation of the method is its agreement with the manual clinical standard for velocity estimation — dividing the vessel length by the visually assessed contrast transit time. The close correlation between automated and manual measurements confirms that the algorithm successfully captures the core hemodynamic event. By automating this process, the algorithm eliminates inter-observer variability and significantly reduces analysis time, moving closer to the goal of real-time, catheter-lab QFR assessment.

References

Вабищевич П. Н., Васильев В. И. Вычислительная идентификация младшего коэффициента параболического уравнения // Доклады академии наук. Математика. — 2014. — Т. 455, № 3. — С. 258–260. — DOI: 10.1134/s1064562414020161

Vabishchevich P. N., Vasil'ev V. I. Computational determination of the lowest order coefficient in a parabolic equation // Doklady Mathematics. — 2014. — Vol. 89, No. 2. — P. 179–181. (Original Russian paper: *Vabishchevich P. N., Vasil'ev V. I.* Vychislitel'naya identifikatsiya mladshego koeffitsienta parabolicheskogo uravneniya // Doklady akademii nauk. Matematika. — 2014. — Vol. 455, No. 3. — P. 258–260.)

Васильев В. И., Кардашевский А. М., Иванов Д. К., Кардашевская К. С. Идентификация нестационарного коэффициента младшей производной в параболическом уравнении // Компьютерные исследования и моделирование. — 2026. — Т. 18, № 3. — С. 607–620.

Vasil'ev V. I., Kardashevsky A. M., Ivanov D. K., Kardashevskaia K. S. Identification of the non-stationary coefficient of the lowest derivative in a parabolic equation // Computer Research and Modeling. — 2026. — Vol. 18, No. 3. — P. 607–620 (in Russian).

Algarni M., Al-Rezqi A., Saeed F., Alsaeedi A., Ghabban F. Multi-constraints based deep learning model for automated segmentation and diagnosis of coronary artery disease in X-ray angiographic images // PeerJ Computer Science. — 2022. — Vol. 8. — P. e993. — DOI: 10.7717/peerj-cs.993

Alves J. R., Berg L. A., Gaio E. D., Rocha B. M., de Queiroz R. A. B., dos Santos R. W. A hybrid model for cardiac perfusion: Coupling a discrete coronary arterial tree model with a aontinuous porous-media flow model of the myocardium // Entropy. — 2023. — Vol. 25, No. 8. — P. 1229. — DOI: 10.3390/e25081229

Andersen B. K., Sejr-Hansen M., Maillard L., Campo G., Råmunddal T., Stähli B. E., Guiducci V., Serafino L. D., Escaned J., Santos I. A., López-Palop R., Landmesser U., Dieu R. S., Mejía-Rentería H., Koltowski L., Žiubrytė G., Cetran L., Adjedj J., Abdelwahed Y. S., Liu T., Mogensen L. J. H., Eftekhari A., Westra J., Lenk K., Casella G., Van Belle E., Biscaglia S., Olsen N. T., Knaapen P., Kochman J., Santos R. C., Scarsini R., Christiansen E. H., Holm N. R. Quantitative flow ratio versus fractional flow reserve for coronary revascularisation guidance (FAVOR III Europe): a multicentre, randomised, non-inferiority trial // The Lancet. — 2024. — Vol. 404, No. 10465. — P. 1835–1846. — DOI: 10.1016/s0140-6736(24)02175-5

Bennar W., Arroyo D., Oppé C., Garin D., Allemann L., Pittet T., Meier P., Puricel S., Togni M., Cook S. Diagnostic accuracy of angiography-derived Murray law-based quantitative flow ratio (μQFR) versus pressure-derived fractional flow reserve (FFR) in moderate to severe calcified coronary lesions — the DIAMOND study // Catheterization and Cardiovascular Interventions. — 2025. — Vol. 106, No. 1. — P. 377–383. — DOI: 10.1002/ccd.31553

Chu J., Lin H., Yan W., Yuan D., Lai Y., Liu X. Angiographic quantitative flow ratio in acute coronary syndrome: beyond a tool to define ischemia-causing stenosis — a literature review // Cardiovascular Diagnosis and Therapy. — 2022. — Vol. 12, No. 6. — P. 892–907. — DOI: 10.21037/cdt-22-334

Conte E., Sonck J., Mushtaq S., Collet C., Mizukami T., Barbato E., Tanzilli A., Nicoli F., De Bruyne B., Andreini D. FFRCT and CT perfusion: A review on the evaluation of functional impact of coronary artery stenosis by cardiac CT // International Journal of Cardiology. — 2020. — Vol. 300. — P. 289–296. — DOI: 10.1016/j.ijcard.2019.08.018

Gao Z., Wang L., Soroushmehr R., Wood A., Gryak J., Nallamothu B., Najarian K. Vessel segmentation for X-ray coronary angiography using ensemble methods with deep learning and filter-based features // BMC Medical Imaging. — 2022. — Vol. 22, No. 1. — P. 10. — DOI: 10.1186/s12880-022-00734-4

Graafen D., Hamer J., Weber S., Schreiber L. M. Quantitative myocardial perfusion magnetic resonance imaging: the impact of pulsatile flow on contrast agent bolus dispersion // Physics in Medicine and Biology. — 2011. — Vol. 56, No. 16. — P. 5167–5185. — DOI: 10.1088/0031-9155/56/16/006

Guan X., Song D., Li C., Hu Y., Leng X., Sheng X., Bao L., Pan Y., Dong L., Jiang J., Xiang J., Jiang W. Functional assessment of coronary artery stenosis from coronary angiography and computed tomography: Angio-FFR vs. CT-FFR // Journal of Cardiovascular Translational Research. — 2023. — Vol. 16, No. 4. — P. 905–915. — DOI: 10.1007/s12265-023-10361-1

Haley H. A., Ghobrial M., Morris P. D., Gosling R., Williams G., Mills M. T., Newman T., Rammohan V., Pederzani G., Lawford P. V., Hose R., Gunn J. P. Virtual (Computed) Fractional flow reserve: Future role in acute coronary syndromes // Frontiers in Cardiovascular Medicine. — 2021. — Vol. 8. — P. 735008. — DOI: 10.3389/fcvm.2021.735008

Hassan A., Sarmun R., Chowdhury M. E. H., Murugappan M., Alqahtani A., Balusamy B., Zoghoul S. B. CASR-Net: an image processing-focused deep learning-based coronary artery segmentation and refinement network for X-ray coronary angiogram // arXiv preprint. — 2025. — DOI: 10.48550/arXiv.2510.27315

He H., Banerjee A., Choudhury R. P., Grau V. Deep learning based coronary vessels segmentation in X-ray angiography using temporal information // Medical Image Analysis. — 2025. — Vol. 102. — P. 103496. — DOI: 10.1016/j.media.2025.103496

Ihdayhid A. R., Norgaard B. L., Gaur S., Leipsic J., Nerlekar N., Osawa K., Miyoshi T., Jensen J. M., Kimura T., Shiomi H., Erglis A., Jegere S., Oldroyd K. G., Botker H. E., Seneviratne S. K., Achenbach S., Ko B. S. Prognostic value and risk continuum of noninvasive fractional flow reserve derived from coronary CT angiography // Radiology. — 2019. — Vol. 292, No. 2. — P. 343–351. — DOI: 10.1148/radiol.2019182264

Kawashima H., Kogame N., Ono M., Hara H., Takahashi K., Reiber J. H., Thomsen B., de Winter R. J., Tanaka K., La Meir M., de Mey J., Schneider U., Doenst T., Teichgräber U., Wijns W., Mushtaq S., Pompilio G., Bartorelli A. L., Andreini D., Serruys P. W., Onuma Y. Diagnostic concordance and discordance between angiography-based quantitative flow ratio and fractional flow reserve derived from computed tomography in complex coronary artery disease // Journal of Cardiovascular Computed Tomography. — 2022. — Vol. 16, No. 4. — P. 336–342. — DOI: 10.1016/j.jcct.2022.02.004

Ko B. S., Cameron J. D., Munnur R. K., Wong D. T., Fujisawa Y., Sakaguchi T., Hirohata K., Hislop-Jambrich J., Fujimoto S., Takamura K., Crossett M., Leung M., Kuganesan A., Malaiapan Y., Nasis A., Troupis J., Meredith I. T., Seneviratne S. K. Noninvasive CT-derived FFR based on structural and fluid analysis // JACC: Cardiovascular Imaging. — 2017. — Vol. 10, No. 6. — P. 663–673. — DOI: 10.1016/j.jcmg.2016.07.005

Li S., Fan Y. Coronary artery segmentation in X-ray angiography based on deep learning approach // 2024 43rd Chinese Control Conference (CCC). — IEEE, 2024. — P. 7345–7350. — DOI: 10.23919/ccc63176.2024.10662007

Lü H., Wang P. A comment on a fast parallel algorithm for thinning digital patterns // Communications of the ACM. — 1986. — Vol. 29. — P. 239–242. — DOI: 10.1145/5666.5670

Martens J., Panzer S., van den Wijngaard J., Siebes M., Schreiber L. M. Influence of contrast agent dispersion on bolus-based MRI myocardial perfusion measurements: A computational fluid dynamics study // Magnetic Resonance in Medicine. — 2019. — Vol. 84, No. 1. — P. 467–483. — DOI: 10.1002/mrm.28125

Martens J., Panzer S., van den Wijngaard J. P. H. M., Siebes M., Schreiber L. M. Analysis of coronary contrast agent transport in bolus-based quantitative myocardial perfusion MRI measurements with computational fluid dynamics simulations // Functional Imaging and Modelling of the Heart. — Springer International Publishing, 2017. — P. 369–380. — DOI: 10.1007/978-3-319-59448-4_35

Nobre Menezes M., Silva J. L., Silva B., Rodrigues T., Guerreiro C., Guedes J. P., Santos M. O., Oliveira A. L., Pinto F. J. Coronary X-ray angiography segmentation using Artificial Intelligence: a multicentric validation study of a deep learning model // The International Journal of Cardiovascular Imaging. — 2023. — Vol. 39, No. 7. — P. 1385–1396. — DOI: 10.1007/s10554-023-02839-5

O'Brien J., Zhang M., Yong A., Psaltis P., Wong D. Diagnostic performance of low frame rate functional angiography-derived quantitative flow ratio (QFR) compared with fractional flow reserve (FFR) // Heart, Lung and Circulation. — 2023. — Vol. 32. — P. S235–S236. — DOI: 10.1016/j.hlc.2023.06.256

Otsu N. A threshold selection method from gray-level histograms // IEEE Transactions on Systems, Man, and Cybernetics. — 1979. — Vol. 9. — P. 62–66. — DOI: 10.1109/TSMC.1979.4310076

Pantos I., Katritsis D. Fractional flow reserve derived from coronary imaging and computational fluid dynamics // Interventional Cardiology Review. — 2014. — Vol. 9, No. 3. — P. 145. — DOI: 10.15420/icr.2014.9.3.145

Peters B., Paul J.-F., Symons R., Franssen W. M., Nchimi A., Ghekiere O. Invasive fractional-flow-reserve prediction by coronary CT angiography using artificial intelligence vs. computational fluid dynamics software in intermediate-grade stenosis // The International Journal of Cardiovascular Imaging. — 2024. — Vol. 40, No. 9. — P. 1875–1880. — DOI: 10.1007/s10554-024-03173-0

Saito T., Misaki M., Shirato K., Takishima T. Three-dimensional quantitative coronary angiography // IEEE Transactions on Biomedical Engineering. — 1990. — Vol. 37. — P. 768–777. — DOI: 10.1109/10.102792

Sato Y., Nakajima S., Shiraga N., Atsumi H., Yoshida S., Koller T., Gerig G., Kikinis R. Three-dimensional multi-scale line filter for segmentation and visualization of curvilinear structures in medical images // Medical Image Analysis. — 1998. — Vol. 2. — P. 143–168. — DOI: 10.1016/S1361-8415(98)80009-1

Sokolov S. Yu., Volchkov S. O., Bessonov I. S., Chestukhin V. V., Kurlyandskaya G. V., Blyakhman F. A. Estimation of blood flow velocity in coronary arteries based on the movement of radiopaque agent // Pattern Recognition and Image Analysis. — 2019. — Vol. 29, No. 4. — P. 750–762. — DOI: 10.1134/s1054661819040163

Svitenkov A., Pavlov I., Chivilikhin S. A one-dimensional model of agent propagation in arterial blood flow // Procedia Computer Science. — 2018. — Vol. 136. — P. 416–424. — DOI: 10.1016/j.procs.2018.08.277

Tao X., Dang H., Zhou X., Xu X., Xiong D. A lightweight network for accurate coronary artery segmentation using X-ray angiograms // Frontiers in Public Health. — 2022. — Vol. 10. — P. 892418. — DOI: 10.3389/fpubh.2022.892418

Tesche C., De Cecco C. N., Baumann S., Renker M., McLaurin T. W., Duguay T. M., Bayer R. R., Steinberg D. H., Grant K. L., Canstein C., Schwemmer C., Schoebinger M., Itu L. M., Rapaka S., Sharma P., Schoepf U. J. Coronary CT angiography–derived fractional flow reserve: machine learning algorithm versus computational fluid dynamics modeling // Radiology. — 2018. — Vol. 288, No. 1. — P. 64–72. — DOI: 10.1148/radiol.2018171291

Tu S., Barbato E., Köszegi Z., Yang J., Sun Z., Holm N. R., Tar B., Li Y., Rusinaru D., Wijns W., Reiber J. H. C. Fractional flow reserve calculation from 3-dimensional quantitative coronary angiography and TIMI frame count // JACC: Cardiovascular Interventions. — 2014. — Vol. 7, No. 7. — P. 768–777. — DOI: 10.1016/j.jcin.2014.03.004

Westra J., Andersen B. K., Campo G., Matsuo H., Koltowski L., Eftekhari A., Liu T., Di Serafino L., Di Girolamo D., Escaned J., Nef H., Naber C., Barbierato M., Tu S., Neghabat O., Madsen M., Tebaldi M., Tanigaki T., Kochman J., Somi S., Esposito G., Mercone G., Mejia-Renteria H., Ronco F., Bøtker H. E., Wijns W., Christiansen E. H., Holm N. R. Diagnostic performance of in-procedure angiography-derived quantitative flow reserve compared to pressure-derived fractional flow reserve: The FAVOR II Europe – Japan study // Journal of the American Heart Association. — 2018a. — Vol. 7, No. 14. — P. e009603. — DOI: 10.1161/jaha.118.009603

Westra J., Tu S., Winther S., Nissen L., Vestergaard M.-B., Andersen B. K., Holck E. N., Fox Maule C., Johansen J. K., Andreasen L. N., Simonsen J. K., Zhang Y., Kristensen S. D., Maeng M., Kaltoft A., Terkelsen C. J., Krusell L. R., Jakobsen L., Reiber J. H., Lassen J. F., Bøttcher M., Bøtker H. E., Christiansen E. H., Holm N. R. Evaluation of coronary artery stenosis by quantitative flow ratio during invasive coronary angiography: The WIFI II study (wire-free functional imaging II) // Circulation: Cardiovascular Imaging. — 2018b. — Vol. 11, No. 3. — P. 892418. — DOI: 10.1161/circimaging.117.007107

Wu Q., Vassilevski Y., Simakov S., Liang F. Comparison of algorithms for estimating blood flow velocities in cerebral arteries based on the transport information of contrast agent: An in silico study // Computers in Biology and Medicine. — 2022. — Vol. 141. — P. 105040. — DOI: 10.1016/j.compbiomed.2021.105040

Xu B., Tu S., Qiao S., Qu X., Chen Y., Yang J., Guo L., Sun Z., Li Z., Tian F., Fang W., Chen J., Li W., Guan C., Holm N. R., Wijns W., Hu S. Diagnostic accuracy of angiography-based quantitative flow ratio measurements for online assessment of coronary stenosis // Journal of the American College of Cardiology. — 2017. — Vol. 70, No. 25. — P. 3077–3087. — DOI: 10.1016/j.jacc.2017.10.035

Yang S., Kweon J., Roh J.-H., Lee J.-H., Kang H., Park L.-J., Kim D. J., Yang H., Hur J., Kang D.-Y., Lee P. H., Ahn J.-M., Kang S.-J., Park D.-W., Lee S.-W., Kim Y.-H., Lee C. W., Park S.-W., Park S.-J. Deep learning segmentation of major vessels in X-ray coronary angiography // Scientific Reports. — 2019. — Vol. 9, No. 1. — DOI: 10.1038/s41598-019-53254-7

Zaffino P., Spadea M. F., De Rosa S. CoroFinder: A new tool for real time detection and tracking of coronary arteries in contrast-free cine-angiography // Journal of Personalized Medicine. — 2022. — Vol. 12, No. 3. — P. 411. — DOI: 10.3390/jpm12030411

Zhang Y., Gao Y., Zhou G., He J., Xia J., Peng G., Lou X., Zhou S., Tang H., Chen Y. Centerline-supervision multi-task learning network for coronary angiography segmentation // Biomedical Signal Processing and Control. — 2023. — Vol. 82. — P. 104510. — DOI: 10.1016/j.bspc.2022.104510

Zhang Y., Zhang S., Westra J., Ding D., Zhao Q., Yang J., Sun Z., Huang J., Pu J., Xu B., Tu S. Automatic coronary blood flow computation: validation in quantitative flow ratio from coronary

angiography // The International Journal of Cardiovascular Imaging. — 2018. — Vol. 35, No. 4. — P. 587–595. — DOI: 10.1007/s10554-018-1506-y

Zhuang B., Wang S., Zhao S., Lu M. Computed tomography angiography-derived fractional flow reserve (CT-FFR) for the detection of myocardial ischemia with invasive fractional flow reserve as reference: systematic review and meta-analysis // European Radiology. — 2019. — Vol. 30, No. 2. — P. 712–725. — DOI: 10.1007/s00330-019-06470-8